

Supplementary information for "Qubit architecture with high coherence and fast tunable coupling"

Yu Chen^{1,*}, C. Neill^{1,*}, P. Roushan^{1,*}, N. Leung¹, M.l Fang¹, R. Barends¹, B. Campbell¹, Z. Chen¹, B. Chiaro¹, A. Dunsworth¹, E. Jeffrey¹, J. Kelly¹, A. Megrant¹, J. Y. Mutus¹, P. J. J. O'Malley¹, C. M. Quintana¹, D. Sank¹, A. Vainsencher¹, J. Wenner¹, T. C. White¹, Michael R. Geller², A. N. Cleland¹, and John M. Martinis^{1†}

¹*Department of Physics, University of California, Santa Barbara, California 93106-9530, USA and*

²*Department of Physics and Astronomy, University of Georgia, Athens, Georgia 30602, USA*

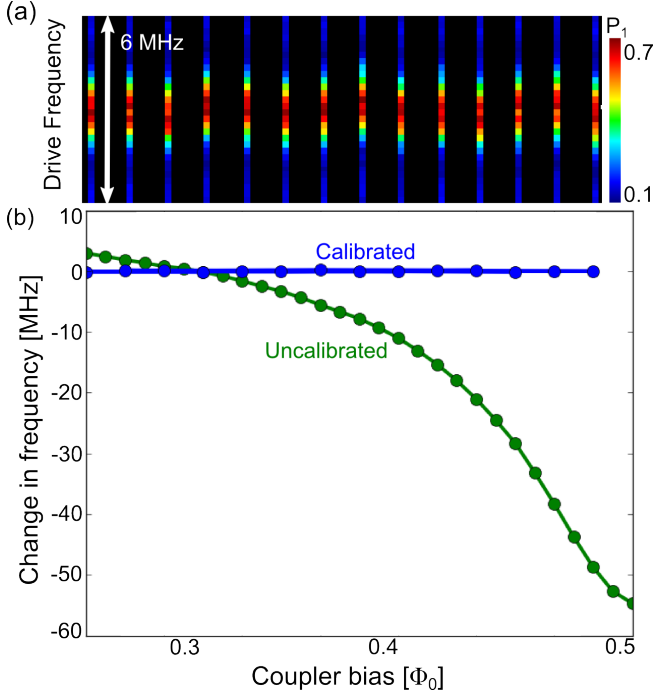


FIG. 1. (a) The frequency of Q_1 , as a function of the coupler flux bias while the second qubit is far detuned. For each value of the coupling strength, we compensate the frequency shift due to the change in inductance, sweep the microwave drive frequency and measure the qubit excited state probability P_1 . Each line is fit for a peak, with the results plotted in panel (b) in blue. The associated standard deviation is 110 kHz. The same experiment is performed without the calibration and overlaid in green.

CALIBRATION

A key aspect of our design is the independent control of the qubit frequency and inter-qubit coupling. The resonance frequency of the individual qubits depends on the impedance of the coupling circuit; this is true for any coupling scheme. In our design, the total qubit inductance L is given by

$$\begin{aligned} L &= L_J + L_g || (L_g + L_c) \\ &= L_J + L_g - M \end{aligned} \quad (1)$$

where $||$ stands for "in parallel with" and M is the mutual inductance given in Eq. (1) of the main text. Changing the inter-qubit coupling is achieved by changing the mutual inductance, which additionally shifts the qubit's resonance frequency. We are able to compensate for this change in inductance using the tunable inductance of the qubit junction L_J . The compensation is achieved by first measuring the qubit frequency ω as a function of the qubit flux bias Φ_Q and then as a function of coupler bias Φ_C . The qubit frequency is given by $\omega = 1/\sqrt{LC} - \alpha$ where C is the qubit capacitance and α is the anharmonicity. Solving this expression for L and using the measured data for ω yields $L(\Phi_C)$ and $L(\Phi_Q)$. From the first expression we determine the change in inductance ΔL due to a change in Φ_C . Using the second expression we calculate the qubit flux bias required to shift L by $-\Delta L$. Summing these two terms yields zero net change in the qubit inductance. Note that the number of measurements required to compensate for the frequency shift scales linearly with the number of qubits and couplers.

The results of this compensation protocol are shown in Fig. 1(a). For each value of the coupler flux bias, we sweep the microwave drive frequency and measure the excited state probability P_1 . The frequency is almost completely independent of the coupler bias, with a standard deviation of 110 kHz. We fit each vertical column of data for a peak and plot the results in blue in Fig. 1(b). We perform an identical measurement without calibration and overlay the results in green. We see that the qubit frequency shifts by over 60 MHz ($\sim g/2\pi$) as we vary the coupler bias.

COHERENCE

The most important part of constructing this tunable coupling architecture is to maintain the coherence inherent in the Xmon design. There are two primary sources of loss associated with the modifications that we have made: capacitive coupling to surface defects on the coupling structure and inductive coupling to the added bias line. The voltage divider created by L_J and L_g reduce capacitive losses by a factor of over 2000. The coupler bias line has a mutual inductance to the junction loop of 1 pH;

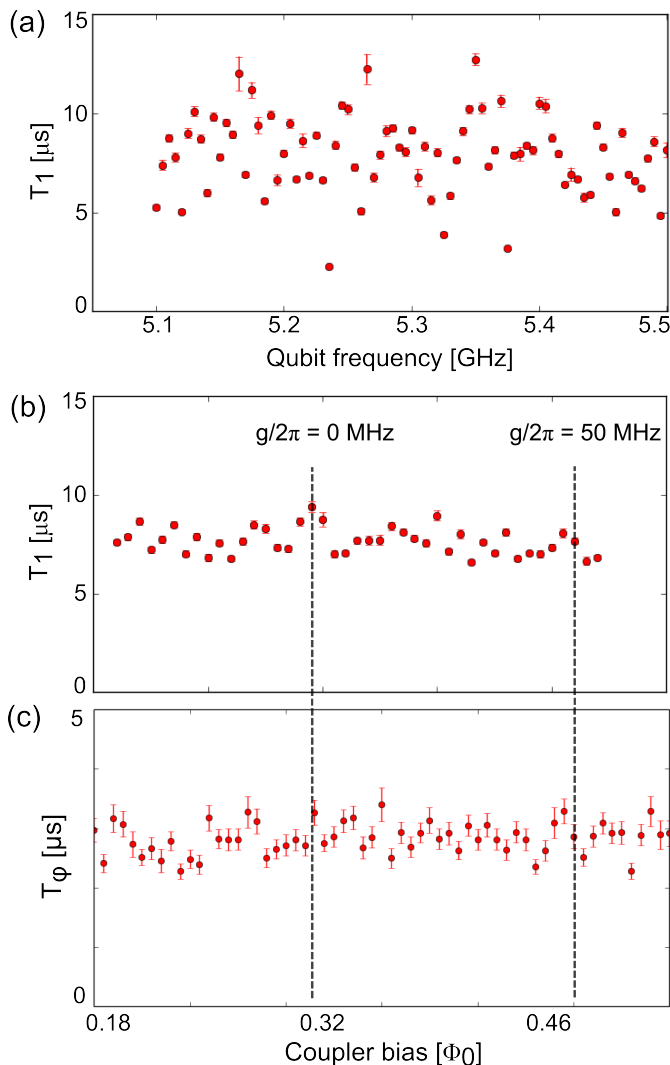


FIG. 2. (a) T_1 of Q_1 as a function of the qubit frequency, when $g = 0$. These results are comparable to that of the Xmon with similar capacitor geometry and growth conditions. (b) T_1 of Q_1 as a function of the coupler bias, when the qubit frequency is set to 5.3 GHz. We find no dependence of the T_1 on the coupling strength.

this 1 pH coupling to a 50 Ohm line introduces a decoherence source with an associated T_1 of greater than 200 μ s at 80 MHz of coupling. We measure T_1 as a function of the qubit frequency and plot the results in Fig. 2(a). These results are comparable to the performance of previous Xmon devices with similar capacitor geometry and growth conditions. We observe no indication that the T_1 is reduced as we vary the coupling strength, with data shown in Fig. 2(b).

It is important to ensure that the coupling circuit does not introduce additional dephasing to the qubits. As discussed in the Ref [1] and [2], the dephasing rate can be minimized by reducing the sensitivity of the qubit frequency to the coupler flux bias, i.e., $df_{10}/d\varphi_{Coupler}$. We have de-

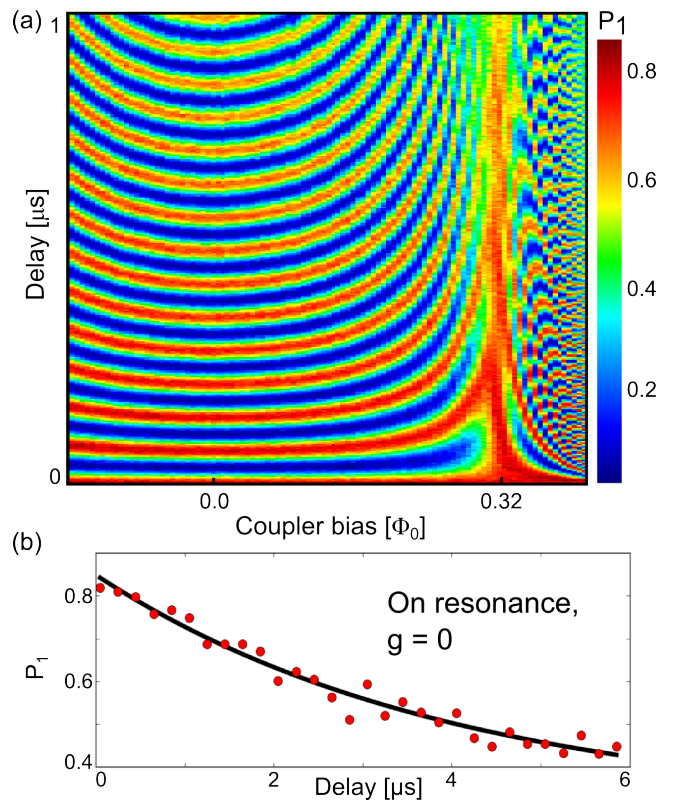


FIG. 3. (a) Swap spectroscopy for Q_1 , as a function of the coupler flux bias, with the two qubits on resonance. For each value of the coupling strength, we excite Q_1 , wait a variable delay time and measure the excited state probability P_1 . We see no excitation swapping between the two qubits when coupler bias is $\sim 0.32\Phi_0$, indicating that the coupling is turned off. (b) We set the coupler bias to this value and examine the excited state probability P_1 of Q_1 over an extended delay time. We see no indication of swapping between the two qubits after 6 μ s (placing an upper bound on residual coupling of 50 kHz.)

signed our gmon with $df_{10}/d\varphi_{Coupler} < 0.1 \text{ GHz}/\Phi_0$, nearly two orders of magnitude less than that of the qubit flux bias $df_{10}/d\varphi_{Qubit}$. As a consequence, near the qubit optimal bias point, we achieved a T_ϕ of 3 \sim 4 μ s over the full range of coupler bias, with data shown in Fig. 2(c). The measured coherence times are comparable to that of Xmon qubits and are independent of the coupler bias. These results demonstrate that our gmon design preserves the high coherence of the Xmon qubit.

ZERO COUPLING

An important application of tunable coupling is to isolate individual qubits for local operations by turning off the coupling. We characterize the zero coupling of our architecture using a modified swap spectroscopy measurement. We bring the two qubits on resonance and vary the

coupler flux bias. For each value of the coupling strength, we excite Q_1 , wait a variable delay time and measure its excited state probability. As the results in Fig. 3(a) show, over a wide range of biases, the two qubits can interact and swap an excitation. At a coupler bias of $\sim 0.32\Phi_0$, there is no excitation swapping between the two qubits, indicating that the coupling is turned off. Focusing on zero coupling, we examine the excited state probability P_1 of Q_1 over an extended delay time, with the results shown in Fig. 3(b). We see no indication of swapping between the two qubits after $6\mu s$. This places an upper bound on residual coupling of 50 kHz, resulting in an on/off ratio > 1000 .

CZ ERROR BUDGET

We perform two measurements to determine the sources of errors in our CZ gate. The dominant contribution to the 0.93% error comes from decoherence. We measure this contribution by performing interleaved randomized benchmarking on a 20 ns two-qubit idle gate, with $g = 0$. We first measure a reference curve without the interleaved idle and plot the data in red in Fig. 4(a). We then perform an interleaved randomized benchmarking sequence in which we insert an idle gate between each random Pauli gate, and overlay the data in blue. Comparing these two curves allows us to extract a fidelity of 99.56% for a 20 ns two-qubit idle gate. Scaling this error rate by a factor of 1.5 to account for the relative length of the CZ yields an error from decoherence of $\sim 0.66\%$.

The next largest contribution to errors are from non-adiabatic transitions from the $|11\rangle$ to $|02\rangle$ state. We directly measure this transition using a Ramsey error filter technique [3]; the pulse sequence is shown inset in Fig. 4(b). We initialize the system in the $|11\rangle$ state and then apply two CZ gates separated by a variable delay time. After applying a π -pulse to each qubit, we measure the uncorrelated excited state probability for each qubit. The results are shown in Fig. 4(b), where we see the expected oscillations that result from the interference between two CZ gates. The frequency of the oscillation is set by the detuning of the $|11\rangle$ and $|02\rangle$ states which was 130 MHz, corresponding to a period of 8 ns. The $|02\rangle$ state leakage error is given as 1/4 of the oscillation amplitude (peak-to-peak). For our 30 ns CZ gate, we measured a non-adiabatic error of $\sim 0.25\%$. This is surprisingly small considering such a short gate time, and can be exponentially suppressed with increasing gate length.

TRANSMON PHYSICS

The operation of the transmon has been previously described in detail [4]. Here, we give a simplified calculation

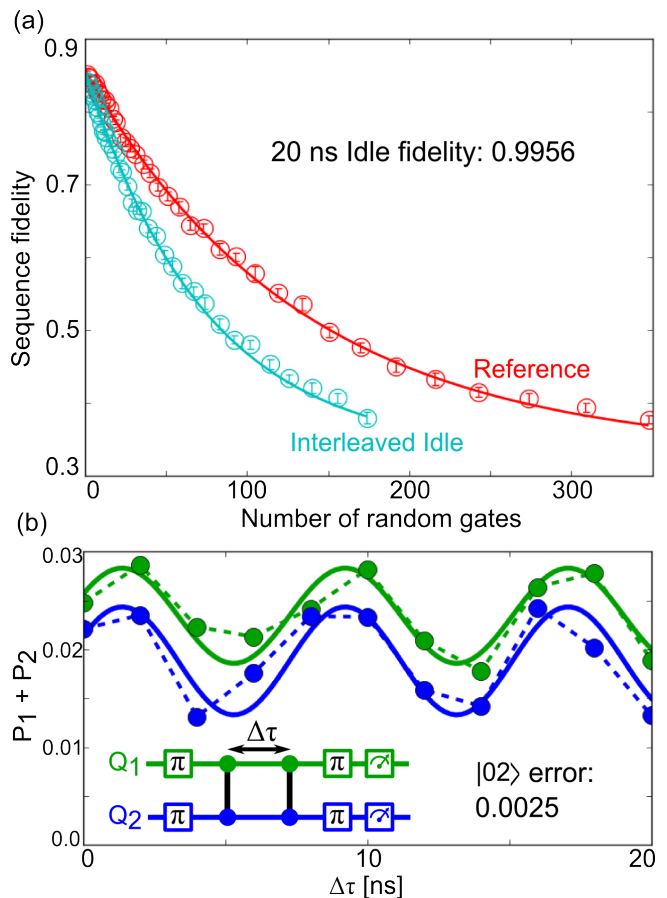


FIG. 4. (a) Interleaved randomized benchmarking on a 20 ns two-qubit idle gate ($g = 0$). We extract a fidelity of 99.56%, which suggests a decoherence error of 0.66% for the 30 ns CZ gate. (b) Inset: The pulse sequence for the Ramsey error filter technique. Main panel: The measured excited state probability $P_1 + P_2$ as a function of the delay between two CZ gates. We observe the expected sinusoidal oscillation with a peak-to-peak amplitude of 1%. The non-adiabatic error from $|02\rangle$ state leakage is 1/4 of the oscillation amplitude and is therefore $\sim 0.25\%$.

in the phase basis that is useful to describe more complex transmon circuits, as for the gmon architecture.

Since the transmon produces qubit behavior from a weak non-linearity, we first review the physics of a linear inductor-capacitor (LC) oscillator. In terms of physical variables charge q and flux Φ , the oscillator Hamiltonian is given by

$$\hat{H}_o = \frac{\hat{q}^2}{2C} + \frac{\hat{\Phi}^2}{2L}. \quad (2)$$

Here the quantum operators of flux and charge obey the standard commutation relation $[\hat{\Phi}, \hat{q}] = i\hbar$. The oscillator frequency is the classical value $\omega = 1/\sqrt{LC}$, and eigenstates m have energy $E_m = \hbar\omega(m + 1/2)$. The ground state wavefunction is given by

$$\Psi_0(\Phi) \propto \exp[-(\omega C/2\hbar)\Phi^2]. \quad (3)$$

Note that the width of the wavefunction is set by the oscillator impedance $Z_o = 1/\omega C = \omega L = \sqrt{L/C}$. Varying this impedance changes the widths of the charge and flux wavefunctions, as illustrated in Table I. The impedance is also important since it is used to describe how strongly the oscillator couples to other modes. The flux and charge operators are conveniently expressed in terms of the raising and lowering operators

$$\hat{\Phi} = (\hbar/2\omega C)^{1/2}(a^\dagger + a) \quad (4)$$

$$\hat{q} = (\hbar\omega C/2)^{1/2}i(a^\dagger - a). \quad (5)$$

For a tunnel junction with shunting capacitor, the charge on the metal island takes on discrete values corresponding to the number of Cooper pairs n . The Hamiltonian for this system is given by

$$\hat{H}_t = 4E_c(\hat{n} - n_g)^2 - E_J \cos \hat{\delta}, \quad (6)$$

where $E_c = e^2/2C$ is the charging energy and $E_J = I_0\Phi_0/2\pi$ is the Josephson energy from the tunnel junction, with critical current I_0 . The normalized coordinates are related to ordinary electrical variables by $\hat{q} = 2e\hat{n}$ and $\hat{\Phi} = (\Phi_0/2\pi)\hat{\delta}$, and thus their commutation relation is $[\hat{\delta}, \hat{n}] = i$. Here we have included a *continuous* charge bias n_g , produced for example by a small coupling capacitor with voltage bias. The Josephson term can be written as $\cos \hat{\delta} = [\exp(+i\hat{\delta}) + \exp(-i\hat{\delta})]/2$, corresponding to number displacement operators $\exp(\pm i\hat{\delta})$ that couple states that differ by one in the number of Cooper pairs.

The form of the solution for this Hamiltonian depends on the ratio of these two energies. For small capacitance where $E_c \gg E_J$, the ‘‘Cooper-pair box’’ limit, the charging energy dominates, and the eigenstates are described by one or the superposition of two number states. The states sensitively depend on the gate charge n_g . This is death to qubit physics, since fluctuations of gate charge from the movement of trapped charge around the junction produces large qubit decoherence from dephasing.

We are interested in the large capacitance ‘‘transmon’’ limit, where $E_J \gg E_c$. Here, the dependence of qubit energy on the gate charge becomes exponentially small, so qubit decoherence from charge fluctuations essentially vanishes. To understand this, note that for large capacitance the phase fluctuations are small. The potential $\cos \hat{\delta}$ can then be expanded in powers of $\hat{\delta}$, with the lowest non-trivial term giving an inductive energy. First considering the case $n_g = 0$, one obtains a harmonic

oscillator-like Hamiltonian

$$H_{to} = 4E_c\hat{n}^2 + (\Phi_0/2\pi)^2\hat{\delta}^2/2L_J, \quad (7)$$

where the Josephson inductance is $L_J = (\Phi_0/2\pi)^2/E_J = \Phi_0/2\pi I_0$. We can thus use harmonic oscillator solutions as the basis eigenstates for perturbation theory.

Note that formally the charge wavefunction is a delta-function comb with spacings $2e$ in charge, with amplitudes given by the harmonic oscillator solution. The charge comb corresponds to a phase wavefunction periodic in 2π . As the capacitance increases, the number of states in the charge wavefunction increases, so that the relative separation of the teeth in the charge comb become so closely spaced as to look like the normal *continuous* solution for the harmonic oscillator. In phase, this implies the wavefunction is so localized in phase that the 2π periodicity does not matter.

The phase wavefunction has a width $\langle \hat{\delta}^2 \rangle$ that can be computed using the exponential term in the wavefunction given by Eq. (3)

$$1 = \frac{\omega C}{\hbar} \left(\frac{\Phi_0}{2\pi} \right)^2 \langle \hat{\delta}^2 \rangle, \quad (8)$$

which gives

$$\begin{aligned} \langle \hat{\delta}^2 \rangle &= \sqrt{8E_c/E_J} \\ &= Z_J/(R_K/8\pi), \end{aligned} \quad (9) \quad (10)$$

where in the last equation $R_K = h/e^2 = 25.8\text{ k}\Omega$ is the resistance quantum, and $R_K/8\pi = 1.026\text{ k}\Omega$. The phase basis works well when the mean quantum fluctuation of the phase is small, which corresponds to a small E_c/E_J ratio or a junction impedance $Z_J = \sqrt{L_J/C}$ much less than $1\text{ k}\Omega$.

The effect of the gate charge n_g in the Hamiltonian can be computed by noting that this offset in the operator \hat{n} can be accounted for by the displacement operator $\exp(in_g\hat{\delta})$ applied to the solution of H_t with $n_g = 0$. This is equivalent to imposing periodic boundary conditions at the phase $\delta = \pm\pi$

$$\Psi(-\pi) = \Psi(\pi) e^{i2\pi n_g}. \quad (11)$$

We can estimate the effect of this boundary condition on the eigenstates by noting that it should be proportional to the probability of the wavefunction at $\delta = \pi$. Using the harmonic oscillator solution, the magnitude of the modulation of eigenstate energy from charge n_g should scale approximately as

$$\Delta E \propto |\Psi_0(\delta = \pi)|^2 \quad (12)$$

$$= \exp[-(\omega C/\hbar)(\Phi_0/2)^2] \quad (13)$$

$$= \exp[-(\pi^2/8)\sqrt{8E_J/E_c}]. \quad (14)$$

We may calculate the exponential factor precisely by including the non-linear junction energy. Using the WKB

TABLE I. Table of relative width of charge and flux wavefunctions as capacitance C (and impedance Z_o) are changed.

C	Z_o	$\langle \hat{q}^2 \rangle$	$\langle \hat{\Phi}^2 \rangle$
small	large	small	large
large	small	large	small

theory, with constants $2m = 1/4E_c$ and $\hbar = 1$ from Eq. (6) and its commutation relation, we find

$$|\Psi_0(\pi)|^2 = \exp\left[-2 \int_0^\pi d\delta \sqrt{(1/4E_c)E_J(1 - \cos \delta)}\right] \quad (15)$$

$$= \exp\left[-\sqrt{8E_J/E_c}\right], \quad (16)$$

matching the result of Ref. [4]. A large E_J/E_c ratio gives exponentially low sensitivity to charge noise.

Note that the phase qubit has vanishing sensitivity to charge noise for two reasons. First, the ratio of E_J/E_c is even larger than for the transmon. Second, the latest versions of the device used a shunting inductor for current biasing. The continuous flow of charge across the junction then shunts any DC change in charge bias. This latter effect is the purpose of the inductor shunt in the fluxonium device.

For completeness, we compute the change in the harmonic oscillator energy eigenvalues due to the cosine non-linearity. Starting from

$$\cos \hat{\delta} \simeq 1 - \hat{\delta}^2/2 + \hat{\delta}^4/24, \quad (17)$$

the correction to the energy from the fourth order term is

$$\Delta E_m = -E_J \langle m | \hat{\delta}^4 | m \rangle / 24 \quad (18)$$

$$= -\frac{E_J}{24} \left(\frac{\hbar}{2\omega C}\right)^2 \left(\frac{2\pi}{\Phi_0}\right)^4 \langle m | (a^\dagger + a)^4 | m \rangle. \quad (19)$$

The matrix element can be calculated by using the square $(a^\dagger + a)^2 = a^{\dagger 2} + a^2 + 2a^\dagger a + 1$, giving

$$\langle m | (a^\dagger + a)^4 | m \rangle = \langle m | a^{\dagger 2} a^2 + a^2 a^{\dagger 2} + (2a^\dagger a + 1)^2 | m \rangle \quad (20)$$

$$= m(m-1) + (m+1)(m+2) + (2m+1)^2 \quad (21)$$

$$= 6m^2 + 6m + 3 \quad (22)$$

where in the first equation we have only kept terms that leave $|m\rangle$ unchanged. The change in energy between adjacent states is

$$\Delta(E_m - E_{m-1}) = -mE_c \quad (23)$$

as expected. As the unperturbed oscillator frequency can be written as $\hbar\omega = \sqrt{8E_J E_c}$, the fractional change in qubit frequency is $\sqrt{E_c/8E_J}$.

Series Inductance

We next consider how this physics changes when including an inductance L in series with the Josephson junction. The total phase across the two elements is given by $\delta = \delta_L + \delta_J$. The conservation of current at the node between the two elements gives the constraint

$I_L = I_0 \sin \delta_J$, which then can be used to relate the individual phase changes and their derivative

$$\delta_L/L = \sin \delta_J/L_{J0} \quad (24)$$

$$d\delta_L/L = d\delta_J \cos \delta_J/L_{J0}, \quad (25)$$

where we have defined $L_{J0} = \Phi_0/2\pi I_0 = (\Phi_0/2\pi)^2/E_J$ as the Josephson inductance at zero current.

The WKB theory gives a charge sensitivity that includes both Josephson and inductor energies

$$-\ln |\Psi_0(\pi)|^2 = \sqrt{\frac{1}{E_c}} \int_0^\pi d\delta \sqrt{E_J(1 - \cos \delta_J) + (\delta_L \Phi_0/2\pi)^2/2L} \quad (26)$$

$$= \sqrt{\frac{E_J}{E_c}} \int_0^\pi d\delta_J [1 + (L/L_{J0}) \cos \delta_J] \times \sqrt{1 - \cos \delta_J + (L/2L_{J0}) \sin^2 \delta_J} \quad (27)$$

$$\simeq \sqrt{8E_J/E_c} (1 - 0.166 L/L_{J0}), \quad (28)$$

where the integral was evaluated numerically. The linear expansion in Eq. (28) is quite good for $L/L_{J0} \leq 1$

The nonlinearity in the energy levels can be evaluated by noting that the quantum fluctuations of the phase is small, so that we can use the linear relation for phase change $\delta_L/L = \delta_J/L_{J0}$. The junction phase can then be found using an inductance divider relation

$$\delta_J = \frac{L_{J0}}{L + L_{J0}} \delta. \quad (29)$$

Following Eq. (19), the change in energy eigenvalues is proportional to $\langle \hat{\delta}_J^4 \rangle = \langle \hat{\delta}^4 \rangle / (1 + L/L_{J0})^4$, giving

$$\Delta(E_m - E_{m-1}) = -\frac{E_J}{24} \left(\frac{\hbar}{2\omega C}\right)^2 \left(\frac{2\pi}{\Phi_0}\right)^4 \frac{12m}{(1 + L/L_{J0})^4} \quad (30)$$

$$= -mE_c \frac{1}{\omega^2 L_{J0} C} \frac{1}{(1 + L/L_{J0})^4} \quad (31)$$

$$= -mE_c \frac{1}{(1 + L/L_{J0})^3}, \quad (32)$$

where for the last equation we have used the resonance condition $\omega^2 = 1/(L + L_{J0})C$. We see that the extra linear inductance lowers the nonlinearity coming from the junction.

* These authors contributed equally to this work

† martinis@physics.ucsb.edu

- [1] John M. Martinis, S. Nam, J. Aumentado, K.M. Lang, and C. Urbina, Phys. Rev. B 67, 094510 (2003).
 [2] Daniel Sank, R. Barends, Radoslaw C. Bialczak, Yu Chen, J. Kelly, M. Lenander, E. Lucero, Matteo Mariantoni, A. Megrant, M. Neeley, P.J.J. O'Malley, A. Vainsencher, H. Wang, J. Wenner, T.C. White, T. Yamamoto, Yi Yin, A.N. Cleland, and John M. Martinis, Phys. Rev. Lett. 109, 067001 (2012).

- [3] Erik Lucero, M. Hofheinz, M. Ansmann, Radoslaw C. Bialczak, N. Katz, Matthew Neeley, A.D. O'Connell, H. Wang, A. N. Cleland, and John M. Martinis, Phys. Rev. Lett. 100, 247001 (2008).
- [4] Jens Koch, T.M. Yu, J.M. Gambetta, A.A. Houck, D.I Schuster, J. Majer, A. Blais, M.H. Devoret, S.M. Girvin, and R.J. Schoelkopf, Phys. Rev. **A** **76**, 042319 (2007).